AUTHOR and OTHER-AUTHOR

[Left hand page running head is author's name in Times New Roman 8 point bold capitals, centred. For more than two authors, write **AUTHOR et al.**]

CONFERENCE PRE-PRINT

Interaction between Geodesic Acoustic Modes and Resonant Magnetic Perturbations in Tokamak Plasmas

J. C. Li*, Z. Lu, J. Q. Xu, Z. Lin, X. D. Lin, J.T. Luo, Y. Liu, C. J. Xiao, J. Q. Dong, Z. B. Shi, W. L. Zhong

Shenzhen Key Laboratory of Nuclear and Radiation Safety, Institute for Advanced Study in Nuclear Energy & Safety, College of Physics and Optoelectronic Engineering, Shenzhen University, Shenzhen 518060, China

Email: lijc@szu.edu.cn

Abstract

An analysis of the statistical spectral characteristics of resonant magnetic perturbations (RMPs), geodesic acoustic modes (GAMs), and their nonlinear coupling with ambient turbulence in the edge region of the HL-2A tokamak has been performed. Experimental observations reveal that RMPs significantly affect low-frequency fluctuations and large-scale turbulence. We present the first direct evidence that increasing RMP current weakens the coupling between GAMs and other frequency modes. Specifically, the amplitude of GAMs decreases as the RMP current increases, with larger RMP currents leading to a more pronounced suppression of GAMs. Moreover, the radial correlation length of turbulence is found to strongly correlate with the increase in RMP current and the reduction of zonal flows. Advanced causal analysis further demonstrates that the radial magnetic field (B_r) and poloidal flows (\tilde{E}_r) exhibit a distinct modulation at a frequency consistent with GAMs, with a phase shift of π , which is modulated by RMP perturbations. These results provide new insights into the impact of RMPs on edge transport, highlighting the dominant role of the interaction between RMP-induced magnetic perturbations, GAMs, and ambient microturbulence in governing edge plasma behavior.

1. INTRODUCTION

In fusion plasmas, the interaction between plasma turbulence and magnetic perturbations has garnered significant attention for understanding and controlling plasma confinement and transport. For instance, neoclassical tearing modes (NTMs) require a seed magnetic island for onset, which can be theoretically triggered by turbulence noise sources. Concurrently, the shear flows induced by magnetic islands can suppress turbulence and play a role in the establishment of internal transport barriers [1-6]. In high-confinement mode (H-mode) plasmas, resonant magnetic perturbations (RMPs) have been widely used to mitigate or suppress edge localized modes (ELMs), and to correct error filed [7-16], recently attracting significant attention within the fusion community [17, 18, 19]. The application of RMPs inevitably induces interactions among magnetic perturbations, microscopic turbulence and zonal flows, ultimately influencing the overall plasma performance [20-26].

Two types of zonal flows are recognized: geodesic acoustic modes (GAMs) and low-frequency zonal flows (LFZFs) [27, 28]. Previous studies have reported the effects of magnetic perturbations on those zonal flows. For instance, GAMs are damped in the presence of resonant magnetic perturbations (RMPs) [29]; magnetic islands induced by RMPs can enhance LFZFs and turbulence at islands' boundaries [30]. Additionally, when the width of the magnetic islands driven by RMPs becomes sufficiently large, the poloidal flow may reverse [31]. Coherent modes, characterized by the interaction between small-scale turbulent activity and localized long-wavelength modes, been detected near low safety factor rational surfaces [32]. Although the theory and application of resonant perturbing magnetic fields are not new concepts [33-35], the plasma's nonlinear behavior in response to RMPs remains intricate, with many unresolved questions. For instance, the role of RMPs in edge turbulence and zonal flows, as well as the synchronization of GAMs with magnetic fluctuations, has been reported [36]. Recently, gas puff imaging measurements have been employed to investigate the interaction between RMPs and edge poloidal flow [37]. On the DIII-D device, beam emission spectroscopy measurements reveal that density fluctuations at microturbulence scales increase directly with the amplitude of the RMP, indicating that magnetic perturbations induced by the RMP influence the regulation of microturbulence on DIII-D. Gyrokinetic simulations further demonstrate that the application of RMP correlates directly with a reduction

[Right hand page running head is the paper number in Times New Roman 8 point bold capitals, centred]

in zonal flow levels, leading to an increase in turbulence fluctuation levels, consistent with experimental observations following the application of RMP.[38]

Despite considerable efforts [39, 40], the experimental understanding as well as the causality analysis of the nonlinear coupling among RMPs, GAMs, and turbulence in the plasma edge region remains crucial for advancing our understanding of the physics of multi-scale interactions. In this paper, we present experimental observations of the nonlinear coupling between RMPs, GAMs, and turbulence, and provide the first experimental evidence demonstrating the nonlinear modulation of turbulence by RMPs.

2. ANALYSIS METHODS

In the domain of plasma computation, a plethora of statistical tools are available for the analysis of random signals. Within signal processing, first-order and second-order statistics are paramount. However, many signals encompass nonlinear processes that cannot be adequately described by these methods alone. Consequently, higher-order statistical methods were developed in the 1960s. High Order Spectrum (HOS), also referred to as polyspectra, has emerged as a crucial tool for the analysis of non-Gaussian linear systems, with the bispectrum being the most significant component of HOS. In the field of plasma science, Kim et al. have developed a bispectrum algorithm specifically designed to analyze the characteristics of turbulent signals in plasma, thereby advancing the analysis of physical signals [41]. The normalized bispectrum can be calculated using the following formula:

$$\hat{b}_{XYZ}^{2}(f_{1},f_{2}) = \frac{|\langle X(f_{1}) Y(f_{2}) Z^{*}(f_{1}+f_{2})\rangle|^{2}}{\langle |X(f_{1}) Y(f_{2})|^{2}\rangle\langle |Z(f_{1}+f_{2})|^{2}\rangle}$$
(1)

where X(f), Y(f) and Z(f) represents the Fourier transform of the signal x(t), y(t) and z(t), and the angle brackets $\langle \rangle$ denote an ensemble average. In the context of X(f)=Y(f)=Z(f), it is referred to as the self-bispectrum.

The bispectrum is defined as follows:

$$\sum \hat{b}_{XYZ}^2(f) = \frac{1}{N} \sum_{f=f_1+f_2} \hat{b}_{XYZ}^2(f_1, f_2)$$
(2)

where the summation $f=f_1+f_2$ is taken over all terms involved.

The two-point correlation technique [43] offers a robust framework for extracting detailed quantitative insights into the structural dynamics of turbulence and zonal flows (ZFs), premised on the assumption that fluctuations can be represented as a superposition of wave packets, each characterized by a stochastic relationship between wavenumber k(f) and frequency f. This method provides a reliable approximation of the local statistical dispersion relation, particularly under conditions where the fluctuation amplitude and wavenumber exhibit minimal variation over a single wavelength. The correlation length (L_c) is determined as the inverse of the spectral broadening in wavenumber space,

$$L_c = 1/\int \overline{\sigma}_k^2 df, \qquad \overline{\sigma}_k^2(f) = \frac{\int \left[k - \overline{k}(f)\right]^2 S(k, f) dk}{\int S(k, f) dk}$$
(3)

where $\bar{\sigma}_k^2(f)$ denotes the width of the wavenumber spectrum. The local wavenumber frequency spectrum,

$$S(k, f)$$
, is defined as $S(k, f) = \frac{1}{M} \sum_{j=1}^{M} I_{\Delta k}[k - k^{j}(f)] |S_{1}^{j}(f) + S_{2}^{j}(f)| / 2$, with $I_{h}(x)$ representing the

indicator function. Here, S_1^j and S_2^j are the power spectra obtained from two spatially separated measurement points, with $\Delta x \leq \pi / k_{\text{max}}$ denoting the separation distance. The parameter k_{max} corresponds to the maximum resolvable wavenumber, while $k^j(f) = \Delta \theta_{12}^j(f)/\Delta x$ is the local wavenumber, $\Delta \theta_{12}^j(f)$ the phase shift between the two points for the j-th realization, and M the total number of realizations. In this study, the poloidal and radial correlation lengths are deduced using floating potential measurements acquired by probe pins with defined poloidal and radial separations.

This paper primarily utilizes spatial correlation and transfer entropy methods to investigate the causal effects of RMPs on edge turbulence and plasma flows. Based on Information Theory, transfer entropy provides a distinctive framework for evaluating causal relationships between time series data. Unlike conventional correlation approaches, it is directional and detects the flow of information between different sequences. This nonlinear technique captures the "transfer of information" between signals, comprising all available data, irrespective of amplitude or sign. Recently, it has been employed in fusion plasmas to quantify the causal influence of zonal flows on turbulence and to analyze the interactions between magnetic islands, zonal flows, and turbulence, showcasing its utility in examining causal dynamics in complex systems[44, 45].

3. RESULTS AND DISCUSSIONS

3.1. Experimental setup

HL-2A is a mid-sized tokamak that utilizes deuterium plasma, typically operating under limiter or lower single null configurations. The device has a major radius of R = 1.65m and a minor radius of r = 0.4m. The heating power is composed of 3 MW from neutral beam injection, 2 MW from lower hybrid current drive, and 5 MW from electron cyclotron resonance heating. Experimental discharge #32654 was conducted under ohmic heating in the limiter configuration. The RMP coil system installed on HL-2A to control ELMs consists of 2 sets of coils near the midplane. Each set of the coils are centered at the poloidal angles $\pm 33.25^{\circ}$, as illustrated in Figure 1(a). The two sets of coils are separated by a toroidal angle of 180° . These four coils are interconnected via a connecting board, allowing for control of the current direction in each coil. The position of the Langmuir probes is located at approximately ρ =0.92. To facilitate the necessary edge plasma measurements, a two-step probe array has been inserted into the outer midplane to measure fluctuations, as depicted in the schematic in Figure 1(b). It is noted that our study was conducted in L-mode without auxiliary heating. Under Ohmic heating conditions, GAM activity is strongest at this location (ρ =0.92), making it particularly well-suited for investigating the interaction between GAM and RMP.

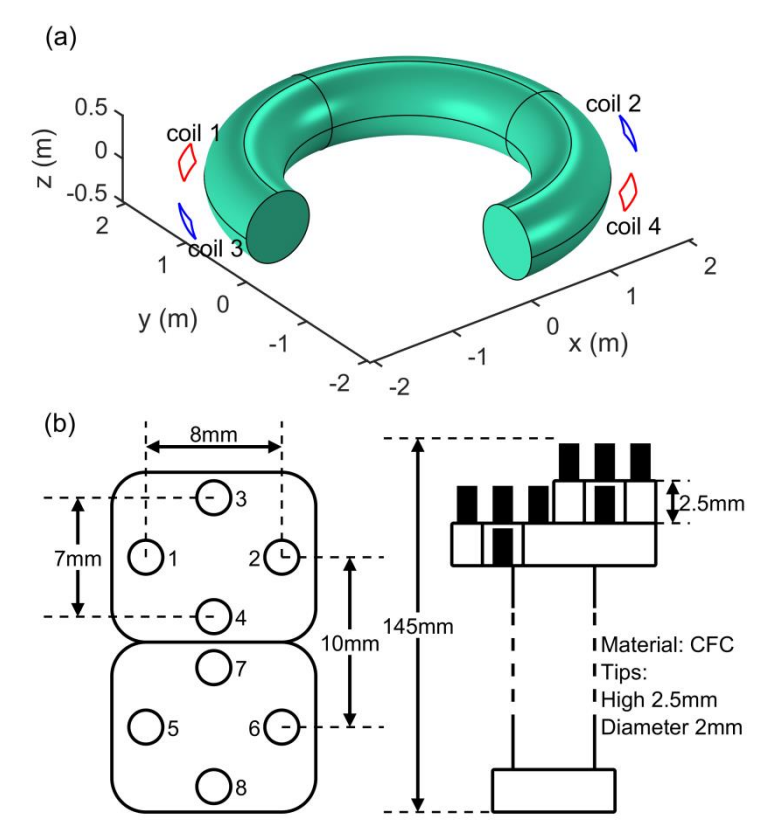


Figure 1. The RMP coils are depicted in blue and red in panel (a), while panel (b) shows a diagram of the fast reciprocating probe array on HL-2A.

In a steady-state scenario, the plasma current Ip=150 kA, with a toroidal magnetic field $B_T=1.36T$ and an average central line electron density of $n_e=1.4\times10^{19} \mathrm{m}^{-3}$. The safety factor at the plasma edge ($\rho=0.92$) is q=4.3. The evolution of plasma temperature and electron density, and the measured radial magnetic fluctuations B_r are shown in Figure 2(a-b). The resonant magnetic perturbation field is configured for n=1 and m=3. The staircase-like coil current waveform, 50 ms in intervals, was programmed to deliver RMP coil current of 0 kA, 2 kA, 3 kA, and 4 kA, as shown in Figure 2(c). The corresponding vacuum radial RMP field is also shown in Figure 2(c). High-speed reciprocating Langmuir probe systems were employed to measure fluctuations in the edge plasma region. The high-frequency magnetic probes measured Br and Br_{rmp} [46,47]. Figure 2(d) presents the floating potential, and its averaged mean values, recorded by one of the probes at $\rho\approx0.92$, with a sampling frequency $f_s=1$ MHz. The temporal and frequency resolved power spectrum the floating potential, obtained by using spectral methods [43], is shown in Figure 2(e).

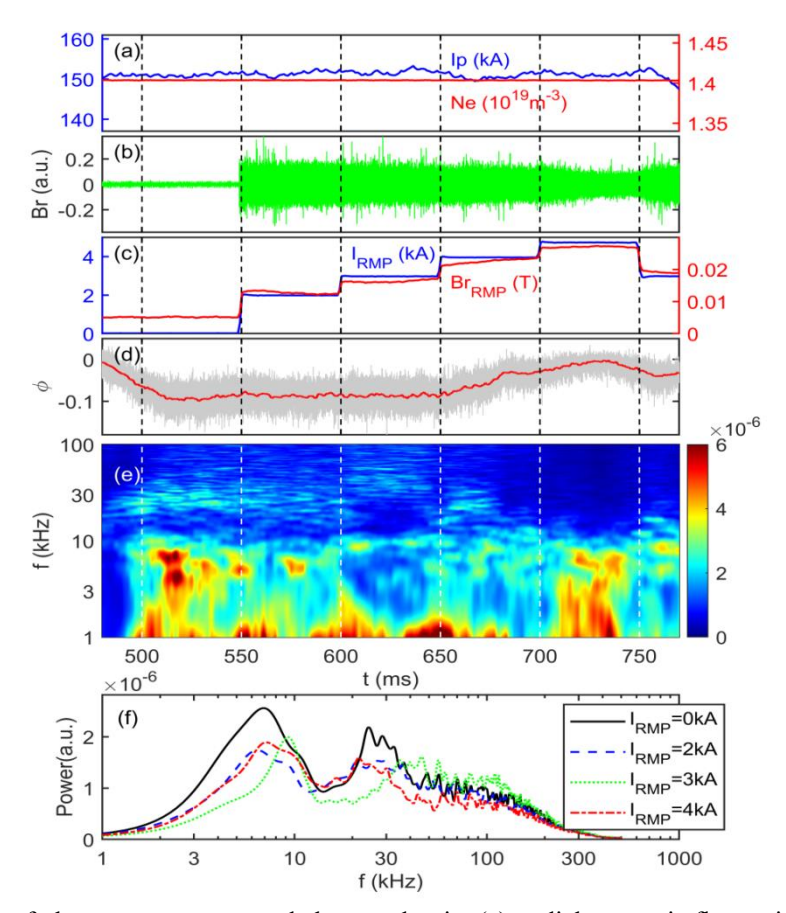


Figure 2. Evolution of plasma temperature and electron density (a), radial magnetic fluctuations B_r (b), RMP current and radial magnetic field (c), floating potential measured by a probe (d), and the time-frequency spectrum of the floating potential (e).

Figure 2(f) displays the power spectral density of the potential fluctuations, at $\rho \approx 0.92$ under varying RMP currents. When the RMP is off, distinct peaks are identified near the GAM frequency of approximately 7 kHz (whose frequencies are consistent with the theoretical prediction that $f_{GAM} \sim c_s \sqrt{2 + 1/q^2}/(2\pi R) = 7.2$ KHz calculated at $T_e \sim 50$ eV) and around 30 kHz. Upon activating the RMP, some shifts of peaking frequency in the power spectra and significant reductions in the peak powers are noted around the GAM frequency near 7 kHz and the ambient turbulence frequency near 30 kHz. In case of $I_{RMP} = 3$ kA, the GAM frequency could be shifted from 7 to 9 kHz. The variation in GAM frequency (from 7kHz to 9 kHz) may be influenced by changes in the local electron temperature (T_e) or the edge safety factor (q_{edge}). Theoretically, an increase in T_e can elevate the GAM frequency by enhancing the sound speed (c_s). Similarly, modifications in q_{edge} could alter the geometric configuration and stability of the plasma edge region, thereby affecting the dynamic characteristics of GAM. Under $I_{RMP} = 3$ kA, the RMP may induce localized perturbations in T_e or T_e or T_e other than the observed frequency shift. Additionally, RMP-induced turbulence amplification or changes in mode structures could also contribute to the frequency variations. Future experiments will aim to test these hypotheses and provide deeper insights into the underlying mechanisms.

3.2 Experimental observations and analysis

We begin by estimating the spectrum of background turbulence to illustrate how turbulent behavior varies under the influence of external fields. The local wavenumber-frequency spectra S(K,f) [46, 47] for conditions with and without RMPs were derived using data from two probes poloidally separated by 7 mm (or 8 mm) at $\rho \approx 0.92$ and are presented in Figures 3(a) and 3(b), respectively. As shown in Figure 3(c), the background turbulence exhibits a dispersion relation characteristic of drift waves rotating in the electron drift direction. When the RMP is off, the power distribution in the spectrum is more concentrated, with higher peak values. Conversely, when the RMP is activated, the wavenumber spectrum becomes relatively flatter, and the peak position shifts toward lower wavenumbers. Figure 3(a-b) also illustrates that the RMP has a significant impact on low-frequency fluctuations (f < 50 kHz) or large-scale turbulence, while high-frequency fluctuations remain largely unaffected. These results from spectral analysis indicate a pronounced influence of RMPs on low-frequency fluctuations

and large-scale turbulence. Fig.3(d) illustrates the statistical dispersion relation $\bar{k}(f)$, derived from the equation $\bar{k}(f) = \sum_k k \cdot s(k|f)$. Additionally, we have calculated the mean wavenumber $\langle k \rangle = \sum_l \bar{k}(f)s(f)$. For $I_{RMP} = 0kA$ and

 I_{RMP} =5kA, $\langle k \rangle$ is 0.3759 and 0.3063, respectively.

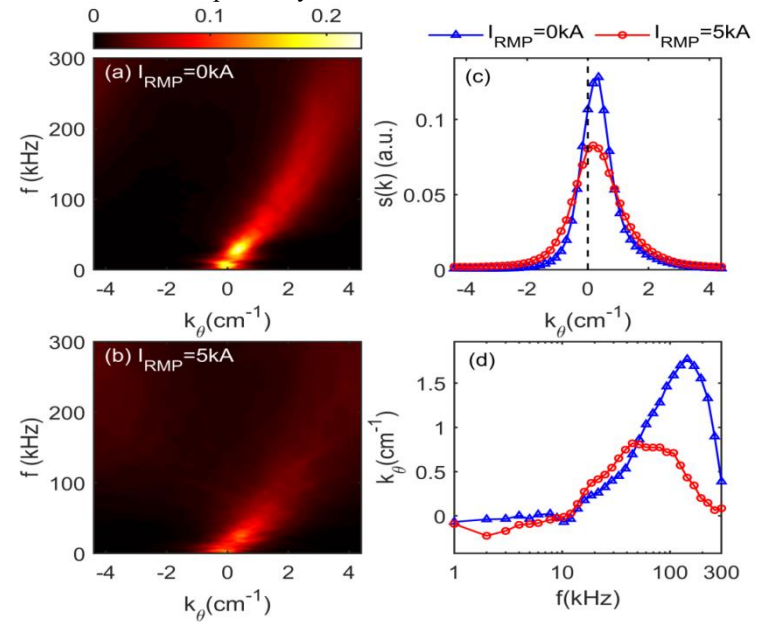


Figure 3. (a) Wave number-frequency spectrum when the RMP is applied $(I_{RMP} = 5kA)$ and (b) when the RMP is turned off. (c) Power spectrum and (d) Wave number spectrum of density fluctuations under both RMP conditions ($I_{RMP} = 0KA, 5kA$).

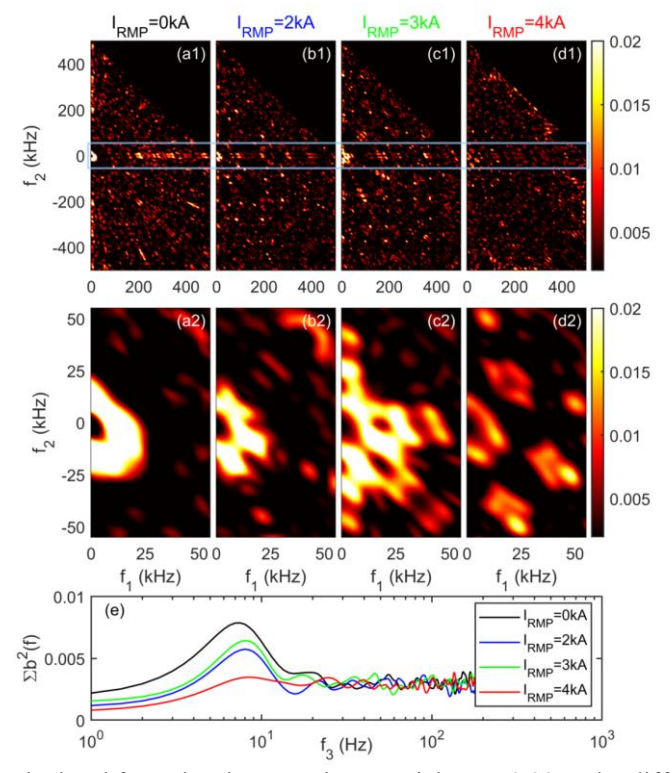


Figure 4. Self-bispectra calculated from the electrostatic potential at $\rho \approx 0.92$ under different RMP currents (a1d1). Panels (a2-d2) present magnified views of the boxed regions in panels (a1-d1), providing enhanced detail. Additionally, panel (e) illustrates the self-bispectrum and cross-bispectrum for comparative analysis.

Figure 4 illustrates the self-bispectrum calculated from the electric potential ϕ at $\rho \approx 0.92$ under different RMP currents. Panels (a1-d1) display the self-bispectra $\hat{b}_{\phi\phi\phi}^2(f_1,f_2)$. Panels (a2-d2) present magnified views of the boxed regions in panels (a1-d1), providing enhanced detail, while panel (e) presents both the self-bispectrum and the

[Right hand page running head is the paper number in Times New Roman 8 point bold capitals, centred]

bispectrum $\sum \hat{b}_{\phi\phi\phi}^2(f)$ (See Appendix). In panel 4(a1, a2), a significant coupling is observed between the ~8 kHz GAM and the turbulence above 200 kHz. However, this coupling diminishes in panels (b1, b2) and (c1, c2), becoming evident only within certain frequency ranges. Specifically, when compared to the RMP-off condition, the coupling between the turbulence over 200 kHz and the GAM is suppressed at RMP currents of 2 kA and 3 kA. In panel 4(d), at an RMP current of 4 kA, the coupling between the turbulence and the GAM nearly vanishes, a trend also reflected in the results presented in panel 4(e). As shown in panel 4(e), the strongest three-wave coupling occurs near 8 kHz when RMP is off. However, this coupling intensity decreases at RMP currents of 2 kA and 3 kA. At 4 kA, the coupling level around 8 kHz is comparable to the noise levels observed at other frequencies, indicating a substantial suppression of the three-wave coupling. Overall, increasing the RMP current appears to weaken the coupling between the GAM and other frequency components.

The impact of RMPs on turbulence is crucial for understanding the multi-scale interactions and the physics of edge turbulent transport under RMP conditions. The long-range correlations are determined by the poloidal correlation length of the GAM, while the transport is primarily governed by the radial correlation length of the turbulence. The poloidal and radial correlation lengths for both GAM and turbulence are depicted in Figures 5(a) and 5(b), respectively. The relationship between the GAM correlation length $L_{\theta,turb}$ and the turbulence radial correlation length L_{r,turb} and the RMP current is not monotonic, reaching a minimum at approximately 5 kA. This indicates that RMP perturbations around this current exert a relatively strong suppressive effect on GAMs. Notably, the poloidal correlation lengths of the GAMs reveal that at I≈3 kA, the correlation length is greater than that at I≈2 kA, suggesting that the GAM exhibits a stronger poloidal correlation in the former case. Overall, as the RMP current increases, the suppressive effect of RMP on GAM transport becomes more pronounced. Conversely, the influence of RMP current on the poloidal correlation length of the turbulence is minimal; as shown in Figure 5(b), only at higher RMP currents does the radial transport of turbulence show some enhancement.

Overall, it is clear that the amplitude of the GAM, denoted by its poloidal correlation length which serves as a measure of the long-range correlation of ZF, is suppressed, except for that a subdominant peak at 3 kA. The underlying reason of this variation with RMP current is not readily apparent and it may be caused by statistical errors as the probe data depends on the relative distance from the pins to the separatrix. However, it is articulated with clarity that, in general, the GAM amplitude decreases with increasing RMP current. The radial correlation length of the GAM shows small variations, which can be understood in terms of the radial wavenumber of the zonal flow being determined by collisional damping; thus, its peak wavenumber tends to remain relatively stable (largely due to minimal changes in temperature and the equilibrium q-profile being approximately constant). In contrast, the increment of radial correlation length ($L_{r,turb}$) of the turbulence is closely related to the increase in RMP current and the corresponding weakening of the zonal flow. This suggests that the increase in radial correlation length of turbulence can be attributed to the GAM suppression. The increase in the L_{r,turb} of turbulence maybe attributed to the fact that the radial magnetic field perturbations provide a new transport particle and energy channel, resulting in enhanced transport propagation, which is reflected in the increased correlation length.

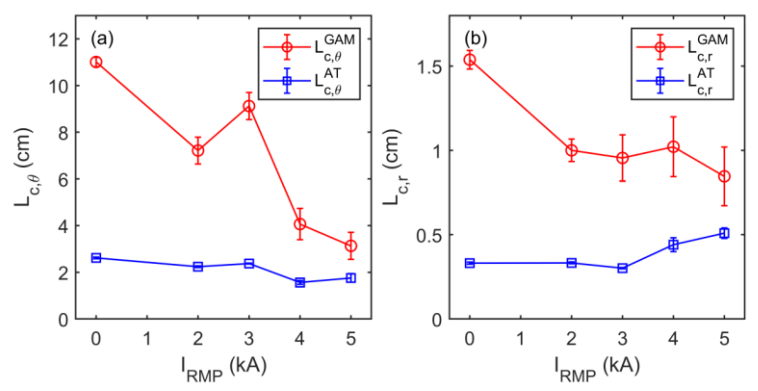


Figure 5. Poloidal (a) and radial (b) correlation lengths of turbulence and GAMs as a function of the RMP current.

CONCLUSIONS

This study analyzes the effects of RMP on GAMs and background turbulence in the edge region of the HL-2A tokamak plasma, focusing on their interactions with GAMs and the nonlinear coupling with ambient turbulence,

AUTHOR and OTHER-AUTHOR

[Left hand page running head is author's name in Times New Roman 8 point bold capitals, centred. For more than two authors, write **AUTHOR et al.**]

as well as the spectral characteristics associated with varying RMP currents. Experimental observations provide the first direct evidence that RMPs has significant effects on low-frequency fluctuations and relatively high-frequency turbulence fluctuations. As the RMP current increases, the RMP weakens the coupling between the GAM and ambient turbulence fluctuations at other frequencies, primarily due to the damping effect of RMPs on GAMs, ultimately leading to a reduction in coupling strength.

Additionally, analysis of the radial and poloidal correlation lengths reveals that the peak power amplitude of the GAM diminishes with increasing RMP current; in particular, higher RMP currents lead to a more significant suppressive effect of RMPs on GAM transport. Furthermore, the radial correlation length $(L_{r,turb})$ of the turbulence is closely linked to the increase in RMP current and the associated weakening of the zonal flow. Overall, RMP appears to enhance transport, which is detrimental to confinement. This is particularly evident in Figure 5(b), where the radial correlation length increases significantly with the rise in RMP current, indicating a pronounced enhancement in transport under these conditions.

ACKNOWLEDGEMENTS

This work was supported by the National Key R&D Program of China under Grant (2024YFE03190003), the Shenzhen International Cooperation Research Project (GJHZ20220913142609017). We would also like to thank Profs. K. Ida, and Z. W. Ma for helpful discussions.

REFERENCES

- [1] AKaw, P. K., Valeo, E. J., & Rutherford, P. H. Phys. Rev. Lett. 43, 1398 (1979).
- [2] Itoh, S. I., Itoh, K., & Yagi, M. Phys. Rev. Lett. 91, 045003 (2003).
- [3] Li, J. et al. Plasma Phys. Control. Fusion 63, 125005 (2021).
- [4] Li, W., Li, J., Lin, Z. et al. Sci Rep 14, 25362 (2024).
- [5] Choi, M. J. et al. Nat. Commun. 12, 375 (2021).
- [6] Li, J. et al. Nuclear Fusion 63, 096005 (2023).
- [7] Kriete, David M., et al. Physics of Plasmas 27.6 (2020).
- [8] Evans, T. E. Plasma Physics and Controlled Fusion 57.12: 123001(2015)
- [9] [9]Orain, F., et al. Physics of Plasmas 20.10 (2013).
- [10] Liu, Y. Q., et al. Nuclear Fusion 51(8) 083002(2011).
- [11] Liu, Y. Q., et al. Plasma Physics and Controlled Fusion 54(12)124013 (2012).
- [12] Callen, J. D. Nuclear Fusion 51(9) 094026(2011).
- [13] Fitzpatrick, R., and T. C. Hender. Physics of Fluids B: Plasma Physics 3(3): 644-673(1991).
- [14] Yu, Q., and S. Günter. Nuclear Fusion 51(7) 073030(2011).
- [15] [15] Park, G., et al. Physics of Plasmas 17.10 (2010).
- [16] Becoulet, M., et al. Nuclear Fusion 52.5 (2012): 054003.
- [17] Willensdorfer, Matthias, et al. Nature Physics 1-9 (2024).
- [18] Kim, SangKyeun, et al. Nature communications 15(1) 3990 (2024).
- [19] Guosheng Xu & Youwen Sun. Islands identified. Nature Physics 20, 1861-1862 (2024) .
- [20] Evans, T. E. et al. Phys. Rev. Lett. 92, 235003 (2004).
- [21] Hasegawa, A., & Wakatani, M. Phys. Rev. Lett. 59, 1581 (1987).
- [22] Li, J. et al. Phys. Plasmas 31, 042502 (2024).
- [23] Zhong, W.L. et al. Rev. Mod. Plasma Phys. 4, 11 (2020).
- [24] Choi, M. J. Rev. Mod. Plasma Phys. 5, 9 (2021).
- [25] Yang, S. et al. Nat. Commun. 15, 1275 (2024).
- [26] Evans, T. E.et al. Nature Phys. 2, 419-423 (2006).
- [27] Diamond, P. H. et al. Plasma Phys. Control. Fusion 47, R35 (2005).
- [28] Conway, G. D., Smolyakov, A. I., & Ido, T. Nucl. Fusion 62, 013001 (2022).
- [29] Robinson, J. R. et al. Plasma Phys. Control. Fusion 54, 105007 (2012).
- [30] Zhao, K. J. et al. Nucl. Fusion 55, 073022 (2015).
- [31] Ida, K. et al. Phys. Rev. Lett. 88, 015002 (2001).
- [32] H. Y. W. Tsui, et al Phys. Rev. Lett. 70, 2565 (1993).

IAEA-CN-316/INDICO ID

[Right hand page running head is the paper number in Times New Roman 8 point bold capitals, centred]

- [33] Xu, Y. et al. Phys. Rev. Lett. 97, 165003 (2006).
- [34] Conway, G. D. et al. Plasma Phys. Control. Fusion 57, 014035 (2014).
- [35] Vlad, M., & Spineanu, F. Nucl. Fusion 56, 092003 (2016).
- [36] Zhao, K. J. et al. Phys. Rev. Lett. 117, 145002 (2016).
- [37] Yuan, J. B. et al. Nucl. Fusion 63, 126017 (2023).
- [38] Williams Z.R. et al. Nucl. Fusion 60, 096004(2020).
- [39] Basu, D. et al. Nucl. Fusion, 58, 024001 (2017).
- [40] Jiang, M. et al. Nucl. Fusion, 59, 046003 (2019).
- [41] Young C. Kim and Edward J. Powers. IEEE. Transactions on Plasma Science PS-7(2), 120-131 (1979). DOI:
- [42] B. Ph. van Milligen, G. Birkenmeier, M. Ramisch, T. Estrada, C. Hidalgo and A. Alonso, Nucl. Fusion 54, 023011 (2014).
- [43] Beall J.M. et al. J. Applied Phys. 53, 3933 (1982).
- [44] Xu, J. Q., et al. Nuclear Fusion 62(8), 086048 (2022).
- [45] Xu, J. Q., et al. Nuclear Fusion 62(12), 126030(2022).
- [46] Cheng Z. et al. Rev. Sci. Instrum. 92, 053518 (2021).
- [47] S.Y. Liang et al. AIP Advances 7, 125004 (2017).